DOI: 10.1007/s11663-007-9050-5

Simulating the Residual Stress in an A356 Automotive Wheel and Its Impact on Fatigue Life

P. LI, D.M. MAIJER, T.C. LINDLEY, and P.D. LEE

Keeping the weight of unsprung rotating components low is critical for fuel efficiency in automobiles; therefore, cast aluminum alloys are the current material of choice for wheels. However, pores formed during solidification can combine with residual stresses and in-service loads to reduce the fatigue life of this safety critical part. In this study, a model of the residual stresses arising from the quench stage of a T6 heat treatment was developed. The resulting predictions were compared to residual strain measurements made on quenched wheels *via* a strain gage/sectioning technique. The predictions were shown to be sensitive to the alloy's flow stress behavior, yet no data were available for the temperature-dependent and strain-rate-dependent inelastic behavior of A356 in the as-solutionized condition. Measurements of this behavior were made using a GLEEBLE 3500, and the data were incorporated into the model, significantly improving the correlation between model and experiment. In order to determine the influence of residual stress upon the final fatigue performance of the wheel during service, the change in stress level due to machining was first calculated. The residual stress was then compounded together with a service stress to determine the local stress at all points in the wheel during idealized operation. Finally, the fatigue behavior was predicted using a unified initiation and propagation model based on this local stress and an idealized pore size.

I. INTRODUCTION

LIGHT weight wheels with good fatigue performance are required to reduce the fuel consumption of transport vehicles, especially as they are unsprung rotating components. Automotive wheels have a complex geometry and must fulfill multiple design criteria: light weight, high strength, good fatigue life, and visual aesthetics. Wheels cast in an A356 aluminum alloy and T6 heat treated fulfill these criteria. Such wheels are typically produced using low pressure die casting, followed by rough machining prior to a T6 heat treatment. Once heat treated, final machining is performed to satisfy dimensional requirements and a multistage paint process is employed to give the desired color and surface finish.

Each of the processing steps (casting, heat treatment, and rough/final machining) can have a significant impact on the component's in-service performance, particularly the fatigue life. The solidification behavior during the casting process defines the initial microstructure and defect distributions. Microsegregation, although partially homogenized during the heat treatment, can reduce the yield strength and thus diminish fatigue life. Pores formed at or in close proximity to the surface can act as crack initiators in the final component.[1,2,3] Rough machining following casting is performed to remove flashing and to control section thicknesses for reduction of thermal gradients during heat treatment. Residual stresses resulting from the casting process can be relieved to some extent by rough machining.

The subsequent T6 heat treatment process is used to improve the mechanical properties of A356 alloy wheels. The T6 heat treatment consists of a solutionizing/homogenizing stage where the component is raised to a temperature of approximately 540 °C to first bring the alloying elements into solution (solutionizing) followed by a holding period for diffusion to reduce microsegregation (homogenization). The component is then quenched in water to obtain a supersaturated solid solution. This step is followed by an artificial aging step at approximately 180 °C, allowing nucleation and growth of Mg-Si precipitates, thereby maximizing the yield strength.

During solutionizing, the residual stresses arising during the previous manufacturing steps (casting and rough machining) should be completely relieved due to the relatively high temperatures and long times. However, during the rapid quench after solutionizing, large thermal gradients occur at high temperatures, resulting in severe plastic deformation due to large thermal strains. This results in residual stresses, which are compressive near the surface and tensile in the core. The residual stresses formed during quench are detrimental for two reasons: (1) they will affect the stress state of the final component, altering fatigue life;[4] and (2) they can cause distortion. These residual stresses may be partially relieved during the aging treatment, so this manufacturing stage must also be studied.[5]

Final machining is performed to achieve dimensional accuracy and to provide clean machined surfaces for aesthetic purposes. However, the removal of the thin layer of compressive surface material can result in tensile stresses at the surface in the final component and may expose larger subsurface porosity, further affecting fatigue performance. Distortion can also occur during the finishing machining operations due to uneven release of these stresses.

P. LI, Ph.D. Student, T.C. LINDLEY and P.D. LEE, Professors, are with the Department of Materials, Imperial College, London, SW7 2AZ, United Kingdom. Contact e-mail: p.d.lee@imperial.ac.uk D.M. MAIJER, Assistant Professor, is with the Department of Materials Engineering, University of British Columbia, Vancouver, BC, V6T 1Z4 Canada.

This article is based on a presentation made in the symposium "Simulation of Aluminum Shape Casting Processing: From Design to Mechanical Properties," which occurred March 12-16, 2006, during the TMS Spring Meeting in San Antonio, Texas, under the auspices of the Computational Materials Science and Engineering Committee, the Process Modeling, Analysis and Control Committee, the Solidification Committee, the Mechanical Behavior of Materials Committee, and the Light Metal Division/Aluminum Committee.

In summary, to accurately predict the fatigue life of a component during service, the manufacturing history must be considered. One way of doing this is to adopt a through process modeling methodology linking the microstructural features and defects to the local stress state arising from both residual stresses and in-service cyclic loads. Although this concept has been proposed previously by the current authors[4,6,7] and others,[8] these prior studies have not determined the sensitivity of the final fatigue life of A356 components to the accuracy of the residual stress calculations, nor were these calculations validated. This article will focus on these aspects.

Several prior authors have modeled the development of residual stresses during quenching in a range of metals (*e.g.,* cast steel,[9] 7010 aluminum alloy forgings,[10,11] and nickel-based superalloy IN718[12]) using sequentially coupled finite element (FE) thermal stress models. A sequential, rather than fully coupled, model is acceptable because the influence of quench-induced deformation on heat transfer is negligible. However, determining the heat-transfer coefficients on the surface of the component is not straightforward, due to the convective flow in the cooling liquid and nucleant boiling. Direct simulation of these phenomena is difficult. Therefore, in several prior studies, the surface-temperature-dependent convection coefficient was empirically determined by matching predictions to measured cooling curves.[10,12]

Having obtained heat-transfer coefficients, these prior studies of residual stresses in Al- and Ni-based alloy forgings[10,12] suggested that the accurate prediction of residual stresses is extremely sensitive to constitutive behavior of the material in the as-solutionized state. The flow stress of the as-solutionized material is also highly temperature and strain rate dependent. For A356, there are very few data available for the as-solutionized state. Most prior measurements are for the fully heat treated or as-cast state. Only one study was found, by Estey *et al.*,[13] who performed a series of isothermal compression tests on A356 samples in the as-solutionized condition over a wide range of temperatures (200 to 500 °C) and strain rates (0.001, 0.1, and 1 s^{-1}) including those experienced during the quenching operation. However, the most important strain rate range during quenching of automotive components was found to be between 0.001 and 0.1 s^{-1}[4]; therefore, more experimental data are required.

In addition to a scarcity of data on the flow stress behavior of as-solutionized A356, there is also a paucity of residual stress measurements in A356 quenched castings against which any residual stress predictions can be validated. Such measurements have been done in other alloys, with the most common technique used for validation being the measurement of residual strain by (1) elastic strain relaxation measurements using mounted strain gages and material removal techniques (*e.g.,* hole drilling,[10] cutting/sectioning, and layer removal) or (2) the interplanar spacing measurement using diffraction methods (*e.g.,* X-ray[10] or neutron diffraction[12]).

The aim of this investigation is to develop a validated model of the residual stress evolution in an A356 automotive wheel during the quench stage of its T6 heat treatment and the redistribution of residual stresses during machining. To achieve this goal, experiments were performed to characterize the temperature- and strain-rate-dependent constitutive behavior of as-solutionized A356. The residual strains in as-quenched and as-aged wheels were measured for model validation. Finally, the validated models were incorporated into a through process simulation of the entire manufacturing chain for an A356 automotive wheel to investigate the effects of quenching parameters, porosity, and in-service loads on their final fatigue performance.

II. EXPERIMENTAL INVESTIGATIONS

A. *Flow Stress*

Isothermal compression tests were performed to measure the flow stress of A356 in the as-solutionized condition as a function of strain, strain rate, and temperature. The series of experiments was designed to cover the temperatures (500 °C down to room temperature) and strain rates (0.001 to 1 s^{-1}) encountered during a typical T6 quench.[4] The experimental parameters and results are given in Table I.

As detailed elsewhere,[3] A356 of similar composition to the wheel (7.25Si, 0.32Mg, 0.06Fe, <0.01Cu, <0.01Mn, <0.01Cr, <0.01Ni, <0.02Zn, <0.01Ti, and <0.01B) was cast into a wedge-shaped permanent mold to create a range of solicitation times, as characterized by the secondary dendrite arm spacing (λ_2). Cylindrical specimens (10-mm diameter × 15-mm high) were sectioned from these castings at different locations to provide different values of λ_2. The specimens used to determine the influence of temperature and strain rate were taken from the central region with a λ_2 of approximately 35 μm. Prior to testing, the specimens were solutionized at 540 °C in an electric resistance furnace for 4 hours and immediately quenched into agitated water at 30 °C and stored at −20 °C to minimize natural aging. The compression tests were performed within 24 hours of solutionizing.

The compression tests were carried out in a GLEEBLE* 3500 thermomechanical simulator using the thermal cycle shown in Figure 1. The specimens were heated at 10 °C/s to a solution temperature of 540 °C and held for 30 seconds following a procedure similar to that used in the previous work.[13] The specimens were then cooled to the compression temperature at a significantly higher cooling rate (20 °C/s instead of 5 °C/s) than that used by Estey *et al*.[13] Upon reaching the testing temperature, the specimens were held isothermally to allow thermal stabilization (Table I for hold times). Compression was then applied to a maximum strain of 0.6.

B. *Residual Elastic Strain Measurements*

To validate the residual stress model, elastic strains were measured at three locations in both as-quenched and as-aged wheels. The wheels (~480-mm diameter) were instrumented with the VISHAY MICROMEASUREMENTS**

---

*GLEEBLE is a registered trademark of Dynamic Systems Inc., Poestenkill, NY.

**VISHAY MICROMEASUREMENTS is a registered trademark of Vishay Intertechnology Inc., Malvine, PA.

Table I. Experimental Parameters and Results for A356 Flow Stress Measurements

Experimental Parameters			Experimental Results (±4 Pct)	
Temperature (°C)	Strain Rate (s^{-1})	Hold Time at Test Temperature (s)	Initial Flow Stress, $\varepsilon = 0.002$ (MPa)	Initial Flow Stress, $\varepsilon = 0.2$ (MPa)
Room temperature	0.01	—	95	255
100		110	66	194
150		60	55	182
200		30	53	159
250		15	51	136
300		15	42	73
350		10	28	39
400		5	21	27
450		5	15	18
500		5	13	15
400	0.001	5	14	17
	0.1	5	29	40
	1	5	37	56
500	0.001	5	7	8
	1	5	24	31
400 ($\lambda_2 = 47$ μm)	0.01	5	25	27
400 ($\lambda_2 = 23$ μm)	0.01	5	23	27

Note: λ_2 is approximately 35 μm unless otherwise stated.

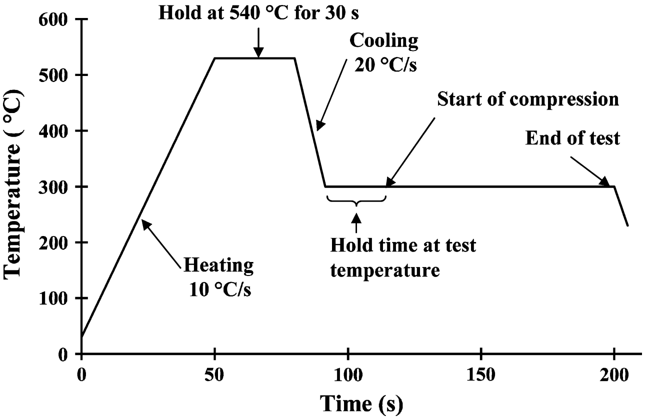

Fig. 1—Thermal cycle of the flow stress experiments using the GLEEBLE 3500.

rectangular rosette strain gages. All the gages had a resistance of 120 Ω ± 0.5 pct, a gage factor of 2.13, and were compensated for aluminum. The gages were mounted using a standardized procedure, as follows. First, the surface was prepared by abrading with sequentially finer sand paper and swabbed with acetone. The strain gage was rinsed with denatured ethyl alcohol, dried, and bonded to the sample's surface using VISHAY MICROMEASUREMENTS** M-Bond 200 adhesive. Pressure was applied for 4 minutes using a Teflon tape interface barrier to prevent bonding between the gages and the pressure applicator. After 24 hours curing time, the gages were soldered to terminal pads using bare lead wires.

The measurements were conducted on a STRAINSERT RT-TN8C† strain indicator using a quarter-bridge circuit configuration. Residual elastic strain measurements were made by (1) initially taking baseline measurements, (2) cutting away as much metal from the gage as possible (leaving a sample ~15-mm square and 5-mm thick), and (3) taking final measurements.

III. MODEL THEORY

A thermal mechanical model was developed (Figure 2) using the general purpose FE program ABAQUS* to predict the final residual stress distribution in the wheel after the two sequential processing steps of quenching and machining. The residual stress relief during artificial aging was neglected. The full wheel was meshed, requiring ~75,000 nodes and ~327,000 linear tetrahedral elements. Linear instead of higher order elements were used to dramatically reduce the computation time (by estimated 10 to 100 times) and memory requirements. Figure 3 shows a 30 deg slice of the model to illustrate the mesh resolution and the amount of material removed during machining (highlighted in white).

A. *Residual Stress Evolution during Quench*

1. *Thermal model*

The thermal phenomena occurring during the T6 quench include (1) heat conduction within the wheel and (2) convective heat transfer between the wheel surfaces and the quench water (55 °C). The thermal history of the wheel during the quench cycle was predicted in a transient heat-transfer analysis by solving the heat conduction equation:

$$\rho \cdot C_p(T) \cdot \frac{\partial T}{\partial t} = \nabla[k(T) \cdot \nabla T] \qquad [1]$$

where T is the temperature, $\rho(T)$ is the density, $C_p(T)$ is the specific heat, and $k(T)$ is the thermal conductivity. Equation

---

†STRAINSERT is a registered trademark of Strainsert Co., West Conshocken, PA.

*ABAQUS is a registered trademark of ABAQUS Inc., Pawtucket, RI.

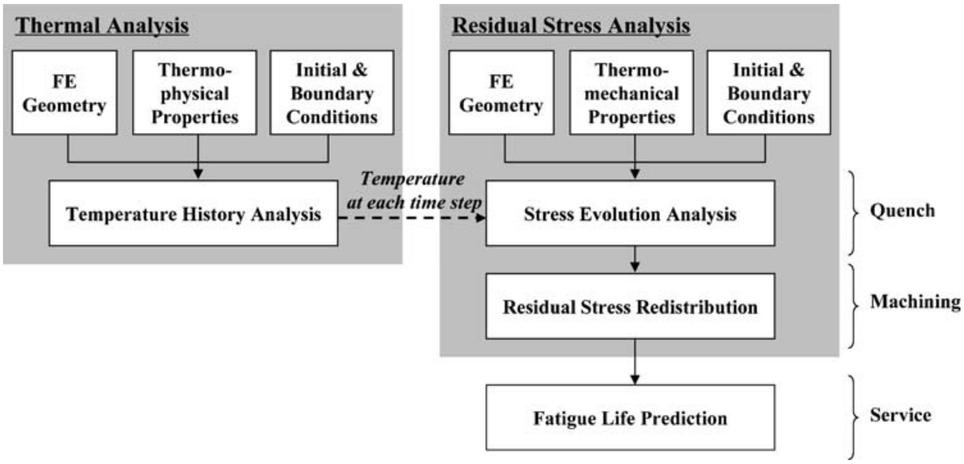

Fig. 2—Flow chart of residual stress model and fatigue life prediction.

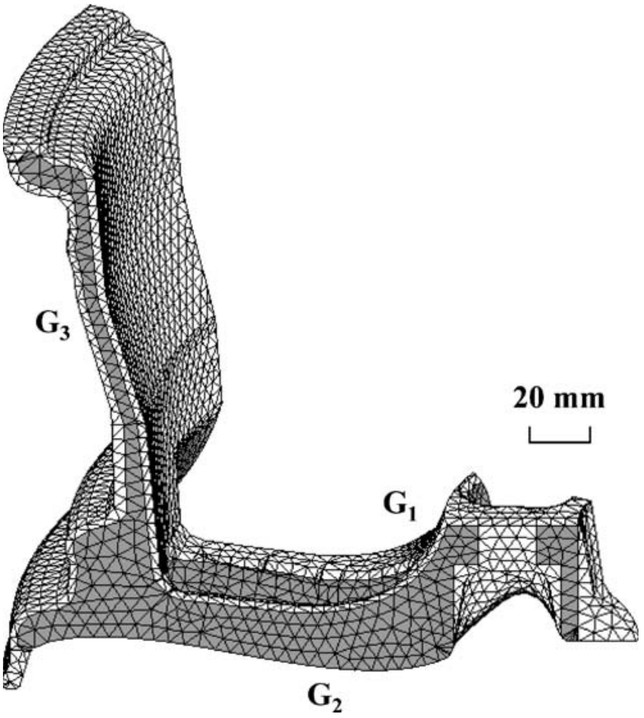

Fig. 3—1/12 section of the wheel mesh used in the FE model including the removed elements (white) during machining. (Note: G_1 to G_3 are strain gage locations.)

[1] is solved by assuming an initial temperature equal to the solution temperature and applying a convective boundary condition to the exposed surfaces of the wheel as

$$q_s = -k\frac{\partial T}{\partial \hat{n}} = h(T_s - T_\infty) \qquad [2]$$

where $h(T)$ is a heat-transfer coefficient and $\hat{n}$ is the outward point direction normal to the surface. Table II lists the temperature-dependent thermophysical property data of A356 used in the model, as obtained from Mills.[14] The heat-transfer coefficient was determined experimentally for a single wheel as a function of the wheel's surface temperature[15] and fitted to the form of equation proposed by Bamberger and Prinz[16] for immersion cooling (Figure 4).

Table II. Material Properties Used in the Model[14]

Temperature (°C)	Thermal Conductivity ($W \cdot m^{-1} \cdot K^{-1}$)	Specific Heat ($J \cdot kg^{-1} \cdot K^{-1}$)	Density ($kg \cdot m^{-3}$)
25	163	880	2680
100	165	921	2662
200	162	967	2641
300	155	1011	2620
380	153	1046	2602
400	153	1055	2600
500	145	1098	2578
567	134	1127	2567

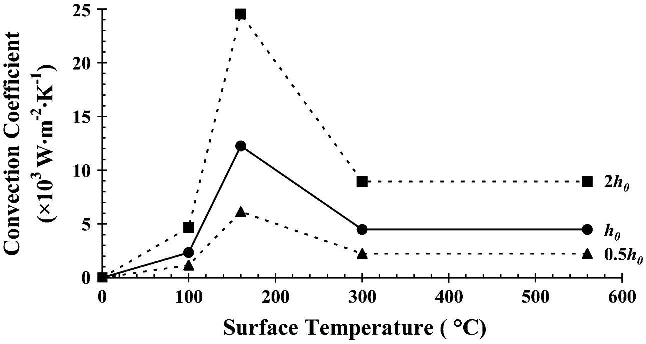

Fig. 4—Convection heat-transfer coefficient as a function of the surface temperature.[16]

The thermal model was also run with half ($0.5h_0$) and double ($2h_0$) the baseline convection coefficient relationship (h_0) (Figure 4) to investigate the sensitivity of residual stress to the quench rate used.

2. *Stress model*

A sequentially coupled thermal stress model was used because the thermally induced deformations during quenching are small with negligible heat generated due to plastic deformation. The temperature history predicted during quench was imposed as a thermal load in the stress model. Thermal strains were calculated using a constant thermal expansion coefficient for A356 of 26×10^{-6} K^{-1}. The total strain ε_t was partitioned into

$$\varepsilon_t = \varepsilon_{th} + \varepsilon_e + \varepsilon_p \quad [3]$$

where ε_{th}, ε_e, and ε_p are the thermal, elastic, and plastic strain components, respectively. The deformation was calculated using isotropic, rate-dependent elasto-plastic constitutive behavior assuming a Mises yield criterion. Elastic properties included the Young's modulus (70 GPa) and Poisson ratio (0.3). The stress-strain data describing the constitutive behavior of A356's flow stress as a function of temperature (up to 500 °C), strain (up to 0.6), and strain rate (0.001, 0.01, 0.1, and 1 s^{-1}) in the as-solutionized condition were determined by linearly interpolating tabulated experimental data from both this study (experimental section) and the work of Estey *et al.*[13]

In order to avoid bulk motion of the wheel, one node was fixed in all directions while the nodes along two perpendicular cut planes passing through the center of the wheel had their displacements fixed normal to the plane.

B. *Residual Stress Redistribution during Machining*

The change in residual stress during machining was simulated by removing the elements corresponding to material cut-off during finish machining from the calculation domain. The stress/strain state in the wheel was then re-equilibrated. The model ignored the inelastic surface strains potentially introduced by the cutting process. The elasto-plastic constitutive behavior for A356 in the final T6 state was measured experimentally using samples taken from the final wheel and fitted as discussed previously.

C. *Fatigue Life Prediction*

Several studies[3,17,18] have investigated the fatigue life of cast aluminum alloys when large pores are present, where large is defined as being greater than the secondary dendrite arm spacing. In this study, the equations developed by two of the current authors with Yi and co-workers were used.[3,17,19] These equations allow the fatigue life N_f to be evaluated using a unified model of crack initiation N_i and propagation N_p for A356-T6 alloys:

$$N_f = N_i + N_p = \frac{C_0}{\lambda_2}\left[\frac{1}{\sigma_a}\left(k_0 + \frac{\alpha}{\sqrt{\lambda_2}}\right)\right]^{2/\beta} + C_1\left(\varepsilon_{max}\frac{\sigma_a}{\sigma_y}\right)^{-s\cdot t}\left(a_f^{-t+1} - a_i^{-t+1}\right) \quad [4]$$

where σ_a is the stress amplitude, $\varepsilon_{\max}$ is the maximum total strain achieved during a loading cycle, σ_y is the yield strength of the material, a_i and a_f are the initial (taken as pore size L) and final (assumed to be 2 mm) crack lengths, respectively. The terms C_0, C_1, k_0, α, β, s, and t are material constants.[17] In this study, the wheel was assumed to have a uniform distribution of secondary dendrite arm spacing, pore size, and in-service stress due to fully reversed cyclic loading, all of which were input into the model as field variables. It was assumed that the residual stress does not alter the service stress amplitude σ_a, because it does not reverse with each cycle. The maximum strain was then calculated with the Young's modulus E according to

$$\varepsilon_{\max} = \frac{\sigma_{\max}}{E} = \frac{\sigma_a + \sigma_r}{E} \quad [5]$$

where the peak stress, $\sigma_{\max}$, is the combined applied load (equal to σ_a) and residual stress σ_γ. Equation [4] was implemented as a user subroutine in ABAQUS to allow mapping of fatigue life as a function of applied and residual stress, maximum pore length, and dendrite arm spacing.

IV. RESULTS AND DISCUSSION

A. *Flow Stress Behavior*

A series of measurements was conducted at temperatures ranging from room temperature to 500 °C at a strain rate of 0.01 s^{-1} (Figure 5 and Table I). The material exhibits hardening at temperatures up to ~300 °C; above this temperature, the flow stress is less sensitive to strain. In the as-solutionized condition, A356 alloy tends to form Mg-Si precipitates that can significantly alter the mechanical properties. Therefore, below 300 °C, Mg-Si particles form and grow, pinning dislocations and enhancing yield strength,[20] as shown in Figure 5. The error in these measurements was determined by performing five repeats at 400 °C (the central condition). Based on the standard deviation in these results, there is an error of ±4 pct.

Another series of measurements was performed to determine the influence of strain rate at temperatures of 400 °C and 500 °C (Table I). As shown in Figure 6, the constitutive behavior of A356 is very dependent on strain rate at high temperature (>300 °C). The flow stress increases with strain rate; moderate hardening is also observed at higher strain rates.

A range of secondary dendrite arm spacing (λ_2) was observed within the wheel (from metallographic examination), which can be related to variations in microsegregation; therefore, the effect of this variation in microstructure upon the flow stress was also investigated. Specimens with the two extremes in λ_2 (23 and 47 μm) were tested at 400 °C with a strain rate of 0.01 s^{-1}. The secondary dendrite arm spacing was found to have almost no effect on the constitutive behavior of A356 alloys at higher temperatures, although previous work[21] suggests that the yield

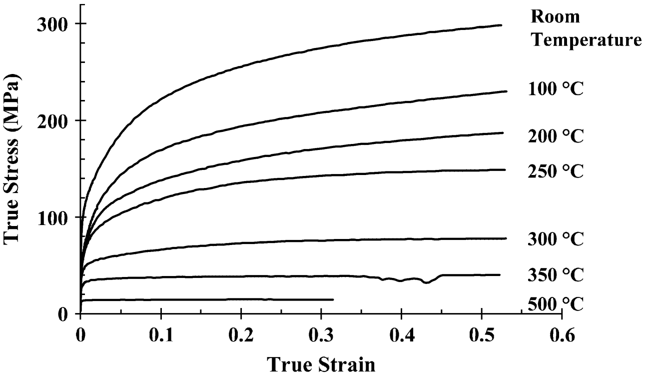

Fig. 5—Flow stress curves at various temperatures (strain rate = 0.01 s^{-1}).

stress increased when λ_2 decreased from 60 to 10 μm at room temperature.

B. *Thermal/Stress Phenomena during Quench*

1. *Evolution of the thermal and stress fields*

The entire wheel cools from the solution temperature (540 °C) to 100 °C in approximately 12 seconds; however, the cooling rate varies depending on the local section thickness (Figure 7). This variation in cooling rates causes adjoining material to have different thermal histories. Figure 8 compares the thermal history between typical surface and core nodes at the rim/spoke joint. This thermal history variation causes thermal gradients, which give rise to residual stresses.

The coupled thermal/stress history can be divided into three stages during quench (Figures 8 and 9).

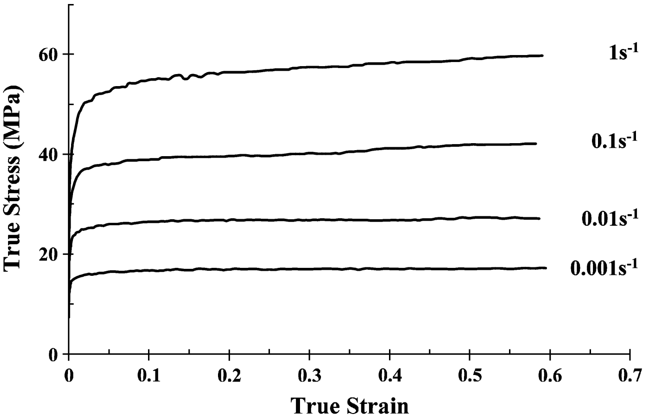

Fig. 6—Flow stress curves at different strain rates (temperature = 400 °C).

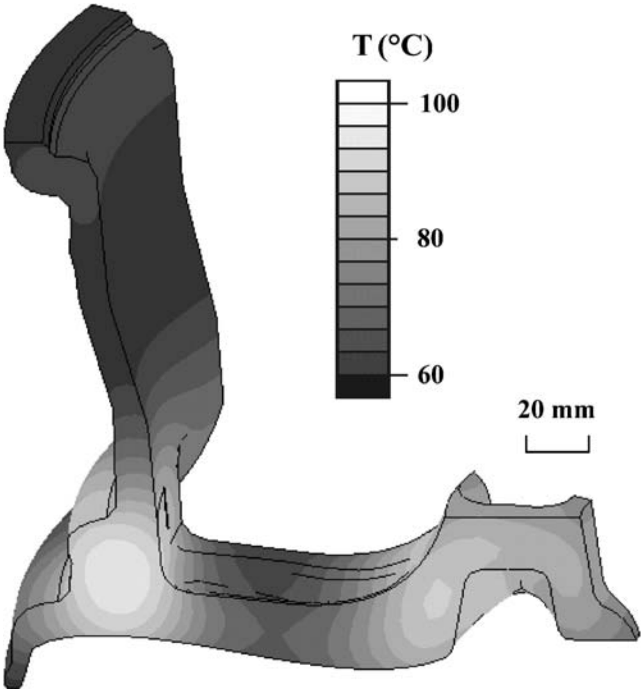

Fig. 7—Temperature distribution at 12 s after the start of quench.

Stage I (<~4 seconds): the wheel surface cools at twice the rate of the core (90 °C/s *vs* 40 °C/s). Due to the higher cooling rate, the surface experiences a greater contraction, which is resisted by the core causing tensile plastic strain to develop on the surface and compressive plastic strain in the core. This stage lasts until the surface reaches a temperature (~200 °C) where it has sufficient strength to resist plastic flow.

Stage II (4 to 8 seconds): the core continues to cool at 40 °C/s to ~200 °C, reducing the thermal gradient in the process as the surface cooling rate decreases to 5 °C/s. During this stage, the core contracts more than the surface, altering its stress state from compressive to tensile, with a balancing compressive state at the surface.

Stage III (>~8 seconds): although the cooling rate differential is much lower (~8 °C and 4 °C/s), the residual stresses continue to accumulate due to the difference in plastic strain and the decrease in thermal gradient between the surface and the core.

The thermal stress evolution during quench reveals that the residual stress state is dominated by the phenomena occurring at the end of stage I (200 °C to 350 °C), when the peak tensile stresses generate plastic strains, which govern the final stress magnitude, although the final residual stress distribution is reversed in sign (Figure 9).

2. *Residual stress distribution*

After the quench operation, the residual stress distribution in the majority of the wheel fits the preceding description,

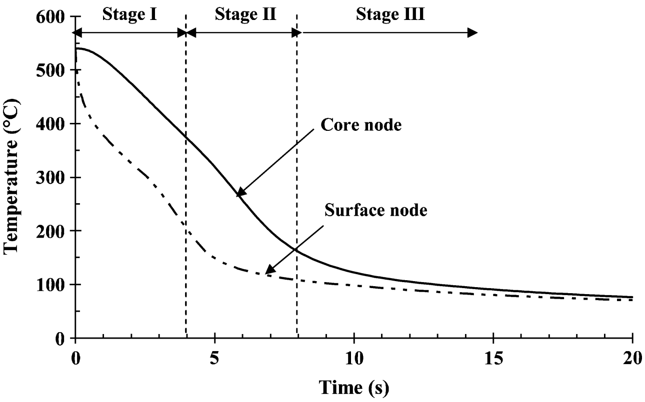

Fig. 8—Temperature history of typical surface and core nodes during quench.

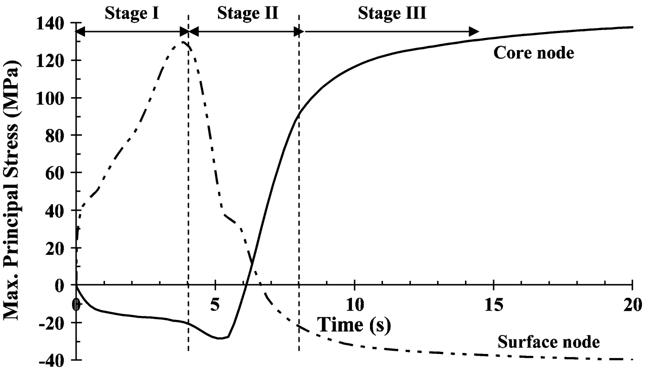

Fig. 9—Stress evolution of typical surface and core nodes during quench.

with a compressive state at the surface and tensile internal residual stress (Figure 10(a)). Tensile residual stresses arise at some surface locations where there is complex geometry (*e.g.,* the inboard surface of location P_2, Figure 10(a)). The magnitude of the residual stress is greater at the thicker sections, which experience larger thermal gradients. The distribution of residual stress is important since surface compressive stresses can improve fatigue performance by inhibiting crack initiation;[3,19] conversely, tensile residual stresses can combine with in-service cyclic loads to reduce fatigue life.

The variation in stress state through the thickness is shown quantitatively in Figure 11 for the two curves marked as P_1 and P_2 in Figure 10(a). Crack initiation sites were found on the inboard surfaces at these locations during the full scale bending (P_1) and radial (P_2) fatigue tests. The residual stress along both of these paths shows the classic transition from large tensile stresses in the core to compression, or nearly compressive, at the surface (note the inboard surface of P_2 is in a state of low tension since it is at the inside of a curved corner). The wheel is thicker at P_2, as compared to P_1; therefore, the residual stresses are larger, ~160 MPa *vs* ~90 MPa.

3. *Effect of quench rate on residual stresses*

In order to investigate the influence of quench conditions on the residual stress, the sensitivity to the convective heat transfer between the component and water bath was studied by doubling ($2h_0$) and halving ($0.5h_0$) the baseline heat-transfer coefficient (h_0). The thermal history of the wheel is significantly affected by the convective heat-transfer phenomena; the wheel cools more quickly due to an increase of quench rate (Figure 12). This indicates that an accurate characterization of the convective boundary condition is critical to the temperature predictions of the quench process. In this study, the baseline heat-transfer coefficient (h_0) was selected based on an investigation where thermocouple data from an industrial facility were compared to model predictions on a geometrically similar A356 wheel.[15] In industrial practice, the wheels are quenched in batches, and there will be some variation about this value depending upon the location and orientation of each wheel.[15]

At $2h_0$, the time to reach 100 °C decreased from ~12 to 8 seconds, leading to enhanced thermal gradients. This causes an increased differential stress during the quench, resulting in higher tensile stresses in the core and increased compressive stresses at the surface (Figure 11). The magnitude of this effect is shown in Figure 13, where the stress variation of typical core (tensile) and surface (compressive) nodes is plotted as a function of the quench heat-transfer coefficient (note: the nodes plotted are the same nodes as in Figures 8 and 9).

The subsurface tensile stresses (>5 mm in depth) increase with the quench intensity, *e.g.,* from 20 to 50 MPa to 30 to 80 MPa in the inboard subsurface at P_1 when h_0 is doubled. Although increasing the surface compressive stress by doubling h_0 may be interpreted as being beneficial to fatigue strength, the simultaneous increase in subsurface tensile residual stress can have adverse effects.

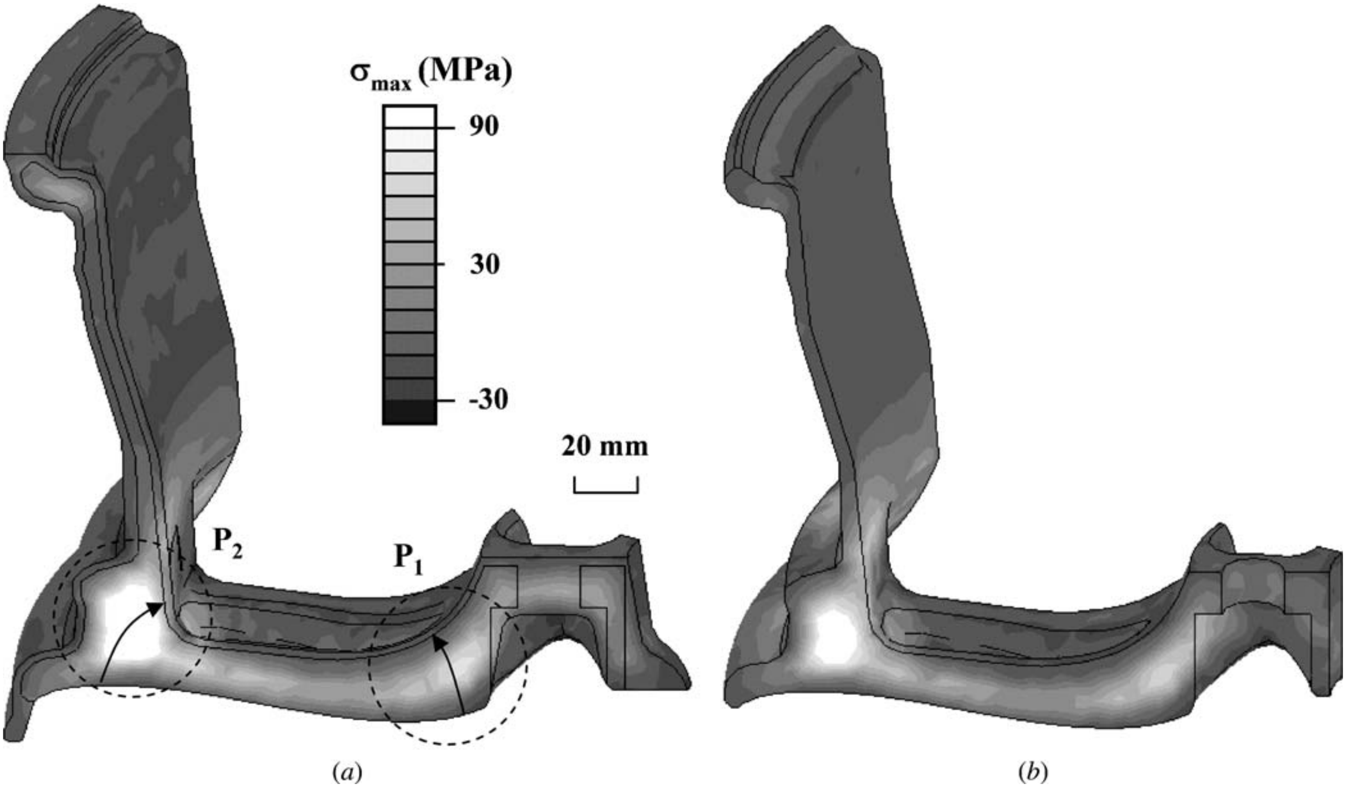

Fig. 10—Residual stress (maximum principal stress) distribution after (*a*) quench and (*b*) machining. (Note: The stresses plotted in Fig. 11 are taken from nodes lying along curves P_1 and P_2.)

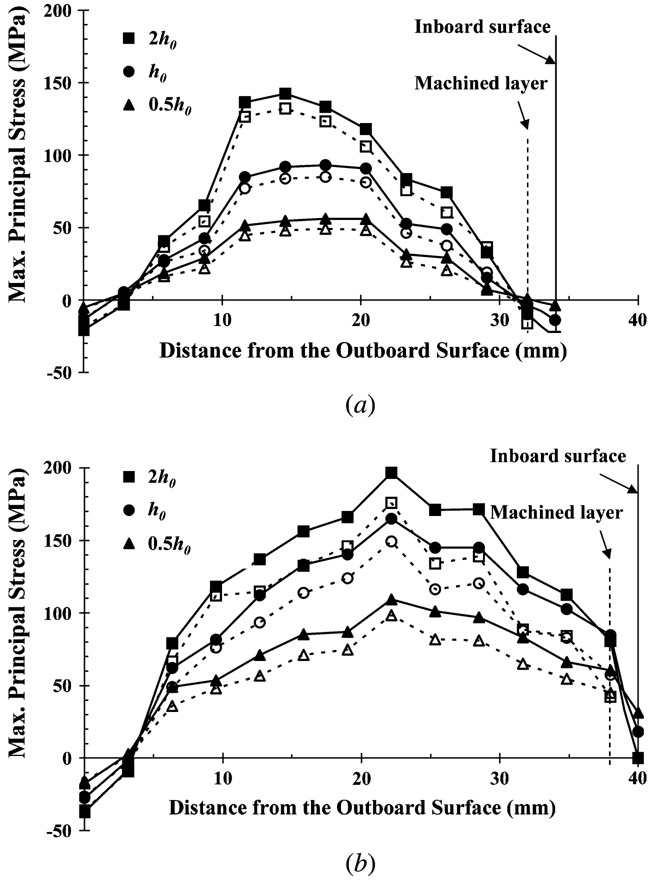

(*a*)

(*b*)

Fig. 11—Variation of residual stresses along the curves (*a*) P_1 and (*b*) P_2 in Fig. 10 for different quench rates: base case (h_0), half the base case ($0.5h_0$), and 2 times the base case ($2h_0$). (Note: solid line/symbols represent after quenching; dashed line/hollow symbols indicate after machining.)

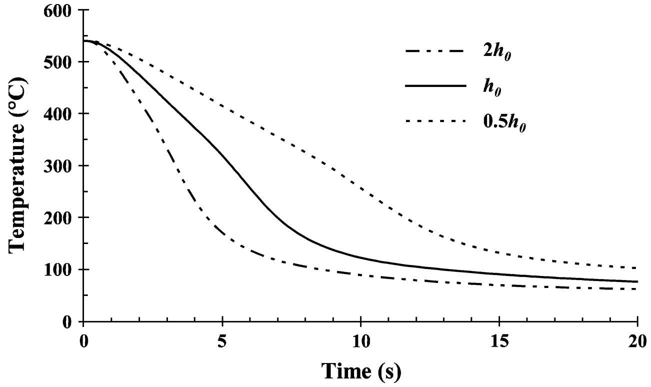

Fig. 12—Temperature history of a typical core node for different quench heat-transfer coefficients.

C. *Residual Stress Relaxation during Machining*

Comparing Figures 10(a) and (b) illustrated that the machining process reduces internal tensile residual stress and reduces the gradient in residual stress. The magnitude of this reduction in the core tensile stress was on the order of 10 to 20 pct, *e.g.,* from 90 to 80 MPa at P_1 and from 160 to 140 MPa at P_2 (Figure 11). Note that the residual stresses were not affected at the outboard surface where machining was not performed. When the compressive surface layer was removed, the majority of newly exposed surface was still in compression, albeit with a reduced magnitude, based on the new equilibrium stress state (Figures 10(b) and 11(a)).

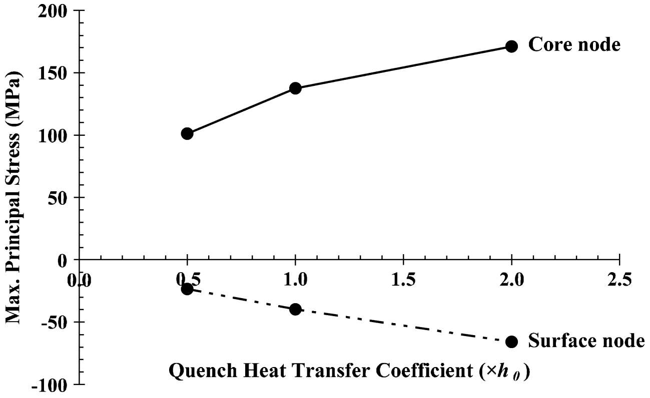

Fig. 13—Quench-induced residual stresses as a function of quench heat-transfer coefficient.

After the material removal and rebalancing of the stress state, subsurface regions in a state of tension (Figures 10(b) and 11(b)) were exposed that may contain pores. The combination of these factors can be highly detrimental to fatigue crack initiation. The tensile residual stress on the inboard surface at P_2 increases from 20 to 60 MPa after the machining operation (Figure 11(b)). The new subsurface (5-mm) tensile residual stress levels are high; they are of the same order as the in-service applied stress, *i.e.,* 20 to 50 MPa at P_1 and 90 to 110 MPa at P_2.

D. *Model Validation*

Elastic strains were measured at locations G_1, G_2, and G_3 (Figure 3) in both as-quenched and aged wheels. These locations were selected because the local residual stress distribution near locations G_1 to G_3 was predicted to be relatively uniform by the model, simplifying analysis of the measurements.

1. *Experimental determination of residual stress relief after T6 aging*

The percentage strain relief η_1 after the T6 aging process was defined as

$$\eta_1 = \frac{\varepsilon_e^{\text{exp(aged)}} - \varepsilon_e^{\text{exp}}}{\varepsilon_e^{\text{exp}}} \times 100 \text{ pct} \qquad [6]$$

where $\varepsilon_e^{\text{exp}}$ and $\varepsilon_e^{\text{exp(aged)}}$ are the measured elastic strains for the as-quenched and as-aged wheels, respectively. The reduction in elastic strain during aging was less than 20 pct (Table III), indicating a small reduction in residual stress. Therefore, due to both the small magnitude of this effect and the absence of the necessary flow stress data to describe the inelastic behavior of A356 alloy during aging, the strain release during the T6 aging process was neglected in the current model.

Table III. Elastic Strain Relief after Aging and Comparison between Measured and Predicted Elastic Strains during the Quench

Locations	Measured			Predicted	
	After Quench	After Aging	Strain Relief	After Quench	Deviation
	($\times 10^{-6}$), ±1 Pct	($\times 10^{-6}$), ±1 Pct	η_1 Pct	($\times 10^{-6}$)	η_2 Pct
G_1	738	689	−7	662	−10
G_2	113	93	−18	132	17
G_3	506	460	−9	354	−30

2. *Residual stress model validation*

The deviation (η_2) between predicted ($\varepsilon_e^{\text{mod}}$) and measured ($\varepsilon_e^{\text{exp}}$) strain was defined to assess the accuracy of residual stress prediction for the quench stage:

$$\eta_2 = \frac{\varepsilon_e^{\text{mod}} - \varepsilon_e^{\text{exp}}}{\varepsilon_e^{\text{exp}}} \times 100 \text{ pct} \qquad [7]$$

The predicted strains are within 30 pct of those measured in the as-quenched wheels (Table III). This represents a good agreement considering that the measurement technique integrates the residual strain of the volume of material attached to the strain gage following sectioning. This illustrates that the residual stress model is sufficiently accurate to represent the quenching process of the wheel.

3. *Sensitivity of model to flow stress data*

In order to evaluate the influence of the accuracy of the constitutive behavior on the residual stress predictions, the model was run with A356 flow stress data from the following conditions: (1) as-cast,[4] (2) as-solutionized, and (3) final T6.[22] The error values $|\eta_2|$ for each case are plotted in Figure 14, demonstrating that the as-solutionized flow stress data offer a more accurate characterization of the quenching process compared to the other conditions, notably in the thin section (G_3) where the relative error is halved.

The marked inaccuracy when using the as-cast and final T6 flow stress curves in the thin region suggests that the inconsistency may arise due to changes in the strain rate sensitivity—the strain rate is the highest in this region and only the as-solutionized data captures this influence accurately. At high strain rates (≥ 0.05 s^{-1}), the as-solutionized flow stresses are substantially different than those in the final T6 and as-cast conditions,[13] causing the increased error at G_3. At low strain rates, the flow stress data are similar for all three conditions,[13] thus reducing the relative error.

E. *Application to Fatigue Life Prediction*

As discussed previously, the tensile residual stress below the surface is on the order of the in-service stress induced during cyclic loading. Therefore, the residual stress contributes significantly to the compounded local in-service stress state, influencing the fatigue performance of the wheel. To illustrate this effect quantitatively, the fatigue life of the wheel was estimated based on the stress state at the inboard and outboard subsurface regions of path P_2 (Figure 10(a)). The variation of fatigue life with the quench intensity, pore size, and service stress amplitude are given in Figures 15 through 17, respectively. The base case values used for these graphs were the quench intensity of h_0, pore size equal to 100 μm, and a 40 MPa service stress amplitude.

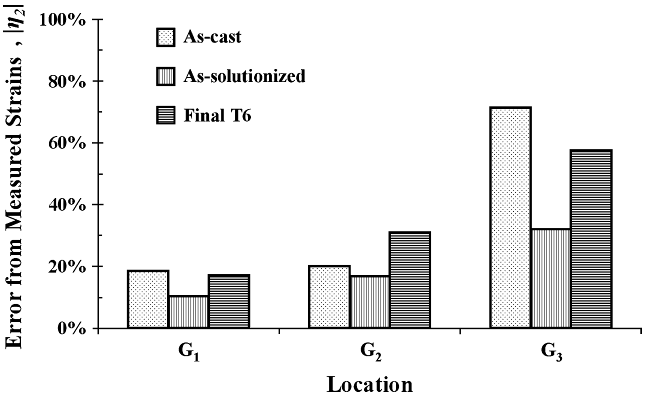

Fig. 14—Comparison of the error between the measured and predicted elastic strains for models using flow stress data obtained from different test conditions.

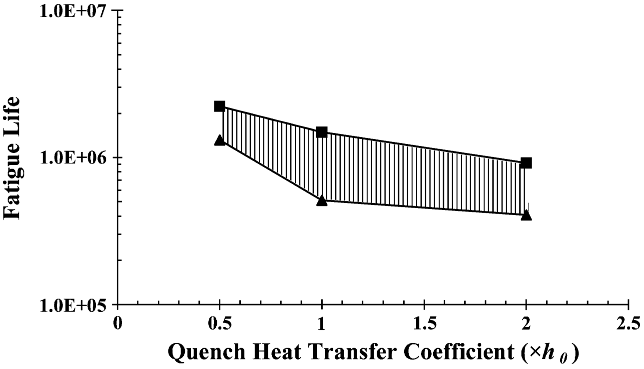

Fig. 15—Predicted fatigue life range as a function of quench heat-transfer coefficient (pore size = 100 μm; service stress amplitude = 40 MPa).

1. *Effect of residual stress*

Figure 15 reveals a moderate effect of quench intensity on fatigue life. Cooling more slowly decreases the magnitude of the residual stresses (Figure 13), causing a concomitant reduction in the compounded local in-service stress, improving fatigue performance. However, quenching slowly can also significantly lower the yield strength of the material achieved after aging by allowing sufficient time for solid solution elements to precipitate rather than remaining supersaturated. A trade-off must therefore be made to optimize the quenching process to achieve high mechanical properties while minimizing residual stresses.

2. *Effect of casting defects*

Figure 16 shows that porosity can significantly influence the fatigue performance of a wheel. If the surface/subsurface pore size is reduced, *e.g., via* grain refining, controlling hydrogen content, or reducing solidification time, the fatigue strength can be enhanced. Similarly, hot isostatic pressing could be performed after casting to close the pores.[23,24] These results are consistent with previous experimental studies.[2,3] Note that a critical value of pore size (~100 μm) is observed in Figure 16, below which fatigue performance can be considerably improved.

3. *Effect of in-service loading*

Figure 17 shows that increasing the applied load reduces the predicted fatigue life, as expected. In this simulation, the propagation life (N_p) takes more than 90 pct of the total fatigue life (N_f), if the total stress amplitude (σ_a) is >120 MPa, while the initiation life (N_i) dominates when σ_a is <90 MPa.

In summary, for this particular component and a fixed service loading, controlling the pore size will provide the most benefit toward improving fatigue performance, with a marked change at a pore size of 100 μm. For a fixed load, Figure 17 illustrates that component redesign to reduce the local stress state (both residual and applied) will also improve fatigue performance. Similarly moving the peak local stress away from regions of high porosity would also improve fatigue performance.

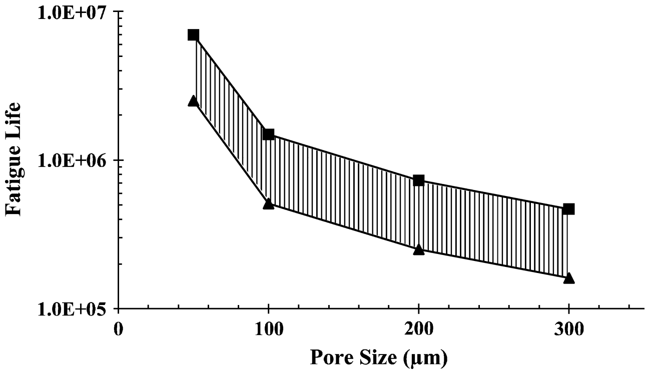

Fig. 16–Predicted fatigue life range as a function of pore size (quench rate = h_0; service stress amplitude = 40 MPa).

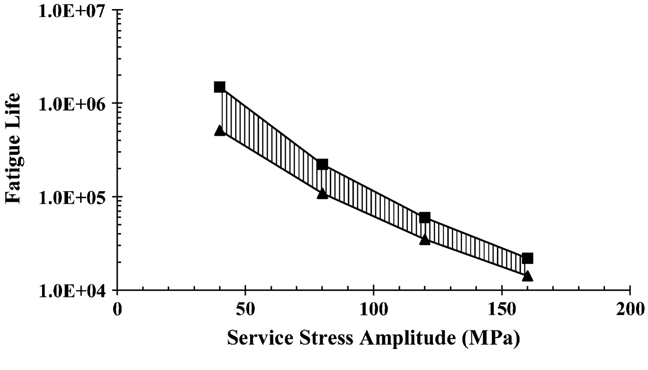

Fig. 17—Predicted fatigue life range as a function of service stress amplitude (quench rate = h_0; pore size = 100 μm).

V. CONCLUSIONS

A mathematical model was developed to predict the residual stress distribution of an A356 alloy wheel, taking into account (1) the residual stress evolution during the T6 quench process and (2) redistribution of residual stress due to material removal at the machining stage.

Isothermal compression tests in a GLEEBLE 3500 were performed to characterize the flow stress of an A356 alloy in the as-solutionized condition. The stress was found to be both temperature and strain rate dependent. Incorporating these data into the model revealed that residual stress predictions are sensitive to the flow stress data. Using the as-solutionized data, the predicted strains matched the measured strains more accurately, halving the error as compared to as-cast data in regions that experience high strain rates during quench (*e.g.,* thin sections).

The quench-induced residual stress evolves mainly between 200 °C and 350 °C, leading to a predicted final stress distribution of compression on the surface and tension in the core. The predicted elastic strains during the quench were in good agreement with those measured using strain gages and sequential sectioning. Subsequent machining relaxed the residual stresses, decreasing their magnitude by 10 to 20 pct. However, the removal of the compressive surface layer exposes areas of tensile residual stress, which will reduce fatigue performance.

The fatigue life of an A356 wheel was predicted by integrating residual stresses into the in-service loading and wheel casting defects (pores). Residual stresses showed a moderate influence on fatigue life for this component—it was more sensitive to casting pore size and service stress due to applied loads.

ACKNOWLEDGMENTS

One of the authors (PL) gratefully acknowledges the financial support of both the Stephen & Anna Hui Fellowship and the Overseas Research Student Award (ORS). The authors also thank C.M. Estey and M.D. Lane, University of British Columbia, for their help during the experiments, and the EPSRC (GR/T26344).

REFERENCES

1. P. Li, P.D. Lee, T.C. Lindley, D.M. Maijer, G.R. Davis, and J.C. Elliott: *Adv. Eng. Mater.*, 2006, vol. 8, pp. 476-79.
2. Q.G. Wang, D. Apelian, and D.A. Lados: *J. Light Met.*, 2001, vol. 1, pp. 73-84.
3. J.Z. Yi, Y.X. Gao, P.D. Lee, H.M. Flower, and T.C. Lindley: *Metall. Mater. Trans. A*, 2003, vol. 34A, pp. 1879-90.
4. D.M. Maijer, Y. Gao, P.D. Lee, T.C. Lindley, and T. Fukui: *Metall. Mater. Trans. A*, 2004, vol. 35A, pp. 3275-88.
5. J.S. Robinson and D.A. Tanner: *Mater. Sci. Technol.*, 2003, vol. 19, pp. 512-18.
6. A. Kermanpur, S. Tin, P.D. Lee, and M. McLean: *JOM*, 2004, vol. 56, pp. 72-78.
7. S. Tin, P.D. Lee, A. Kermanpur, M. Rist, and M. McLean: *Metall. Mater. Trans. A*, 2005, vol. 36, pp. 2493-504.
8. European FP5 Programs G5RD-CT-2000-00153, 1999, http://www.eaa.net/downloads/virprojects.pdf.
9. C.H. Gur and A.E. Tekkaya: *Mater. Sci. Eng., A*, 2001, vols. 319-21, pp. 164-69.
10. D.A. Tanner and J.S. Robinson: *Exper. Mech.*, 2000, vol. 40, pp. 75-82.
11. D.A. Tanner and J.S. Robinson: *Finite Elem. Anal. Des.*, 2003, vol. 39, pp. 369-86.

12. D. Dye, K.T. Conlon, and R.C. Reed: *Metall. Mater. Trans. A*, 2004, vol. 35, pp. 1703-13.
13. C.M. Estey, S.L. Cockcroft, D.M. Maijer, and C. Hermesmann: *Mater. Sci. Eng., A*, 2004, vol. 383, pp. 245-51.
14. K.C. Mills: *Recommended Values of Thermophysical Properties for Selected Commercial Alloys,* Woodhead Publishing Limited, Cambridge, United Kingdom, 2002, pp. 43-49.
15. C.M. Estey: Master's Thesis, University of British Columbia, Vancouver, 2004.
16. M. Bamberger and B. Prinz: *Mater. Sci. Technol.*, 1986, vol. 2, pp. 410-15.
17. J.Z. Yi, Y.X. Gao, P.D. Lee, and T.C. Lindley: *Mater. Sci. Eng., A*, 2004, vol. 386, pp. 396-407.
18. M.J. Caton, J.W. Jones, and J.E. Allison: in *Fatigue Crack Growth Thresholds, Endurance Limits, and Design,* ASTM STP 1732, J.C. Newman, Jr. and R.S. Piascik, eds., ASTM, West Conshohocken, PA, 2000, pp. 285-303.
19. Y.X. Gao, J.Z. Yi, P.D. Lee, and T.C. Lindley: *Acta Mater.*, 2004, vol. 52, pp. 5435-49.
20. U.F. Kocks and H. Mecking: *Progr. Mater. Sci.*, 2003, vol. 48, pp. 171-273.
21. W.R. Osorio, C.A. Santos, J.M.V. Quaresma, and A. Garcia: *J. Mater. Proc. Technol.*, 2003, vols. 143–144, pp. 703-09.
22. H.R. Voorhees and J.W. Freeman: *Report on the Elevated-Temperature Properties of Aluminum and Magnesium Alloys,* ASTM, Philadelphia, PA, 1960, pp. 217-24.
23. P.D. Lee, A. Chirazi, R.C. Atwood, and W. Wang: *Mater. Sci. Eng., A*, 2004, vol. 365, pp. 57-65.
24. P.D. Lee and J.D. Hunt: *Acta Mater.*, 1997, vol. 45, pp. 4155-69.